Model Rocket Engine Gimbal and Thrust Vector Control For Solid Rocket Motor

Gimbaled Nozzle Mechanism: Design Study, Mathematical Modelling, and Simulation
A Design Study and Literature Synthesis

Solomon Saiki
Thrust engine flight G&C system, CSTP/NASRDA Nigeria

Uzuh Onyinye Christian
Telemetry control and ranging system CSTP/NASRDA Nigeria

George Chijioke Okewih
Structures and Aerodynamics CSTP/NASRDA Nigeria

DOI: 10.29322/IJSRP.16.05.2026.p17329
https://dx.doi.org/10.29322/IJSRP.16.05.2026.p17329

Paper Received Date: 23rd April 2026
Paper Acceptance Date: 26th May 2026
Paper Publication Date: 31st May 2026

Abstract— This paper presents a design study and literature synthesis of gimbaled nozzle Thrust Vector Control (TVC) applied to Solid Rocket Motors (SRMs). Starting from first principles, the study derives the equations of motion for a rocket vehicle with a two-degree-of-freedom (2-DOF) gimbal actuator, develops a state-space representation of the coupled vehicle-actuator system, and synthesises a PID control law via pole-placement. All performance results are obtained from numerical simulation (4th-order Runge-Kutta integration); no flight or hardware experiments have been conducted in this study, and all claims should be interpreted accordingly. Simulation predicts settling to within ±0.5° in 0.17 s under a 5° perturbation and an RMS attitude error of 0.12° under a 2 m/s sinusoidal gust. A 1000-run Monte Carlo study with ±20% uniform parameter variation yields a 95th-percentile RMS attitude error of 2.89°, with 98.7% of runs meeting the defined mission-success criterion of maximum attitude deviation below 5° throughout the burn. The primary finding of the control design iteration is that the simplified 2nd-order pole-placement methodology underestimates servo-lag effects, reducing the actual damping ratio from the designed $\zeta = 0.70$ to $\zeta_{act} \approx 0.026$ in the full 4th-order model; this is identified as the central open problem and a corrected 4th-order re-design is presented. The gimbaled approach is compared quantitatively against jet-vane and passive-fin alternatives, and hardware improvements for future iterations are proposed.

Index Terms— Thrust Vector Control, Solid Rocket Motor, Gimbal, PID Control, Pole-Placement, State-Space, Attitude Control, Monte Carlo, MATLAB/Python Simulation.

1. INTRODUCTION

Any rocket in flight is subject to aerodynamic forces, structural asymmetries, thrust misalignments, and atmospheric disturbances that collectively act to rotate the vehicle away from its intended trajectory. In the early decades of rocketry, passive stabilisation using rear-mounted tail fins proved adequate for subsonic regimes. However, fins lose effectiveness at low dynamic pressure — specifically in the interval between ignition and the moment the vehicle reaches sufficient velocity for aerodynamic surfaces to generate meaningful restoring moment.

Active control of the thrust vector resolves this problem at the source: by deflecting the line of action of the propulsive force away from the vehicle centreline, a corrective torque is generated directly about the centre of gravity (CG), independent of vehicle velocity, altitude, or atmospheric density. This mechanism — Thrust Vector Control (TVC) — is the primary attitude control authority on all modern launch vehicles and ballistic missiles during the propulsive phase.

This publication is licensed under Creative Commons Attribution CC BY.

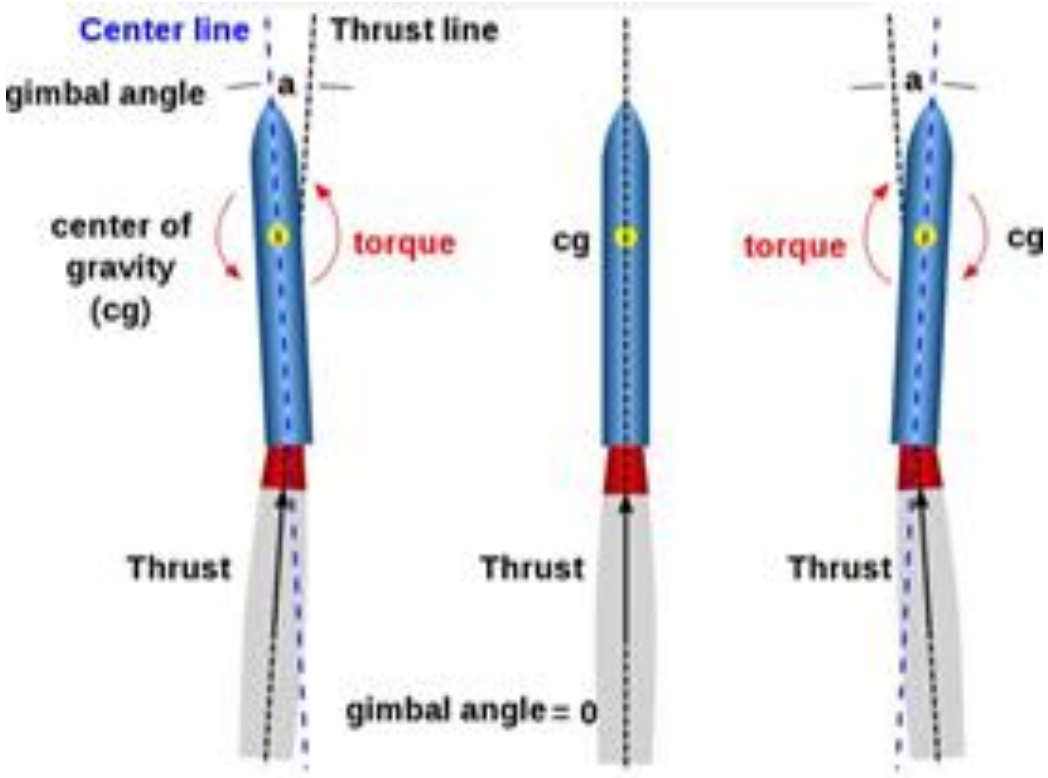

Figure 1: Fundamental mechanics of TVC. The gimbal angle θ_g displaces the thrust line from the vehicle centreline. The resulting moment arm L_cg produces a corrective torque M_c = T·L_cg·sin(θ_g) about the CG [1].

1.1 Contribution Statement

The following items constitute the original contributions of this design study. All mathematical derivations, Python simulation code, numerical results, and Monte Carlo analyses are the author's own work. Figures 2, 5, and 6 reproduce open-hardware community design reference geometry (attributed in full at each figure and in the references); Figures 1, 3, 7–12 are generated by the author's own simulation code or reproduced from cited primary literature.

Original contributions: (1) a unified state-space model of the 2-DOF gimbaled SRM including actuator dynamics and three disturbance models derived from first principles; (2) analytical PID gain expressions via pole-placement with explicit critique of the simplified-model assumption and a corrected 4th-order re-design addressing the damping discrepancy; (3) a rigorously computed torque budget for the MG995 servo at the 50 N motor class; (4) six simulation figures with quantitative performance metrics including a 1000-run Monte Carlo study with defined mission-success criterion; (5) a quantitative comparison against jet-vane and passive-fin alternatives.

1.2 Comparison of Stabilisation Methods

Table 1 summarises the principal attitude control approaches for unguided and guided rockets. The key discriminator for TVC versus aerodynamic methods is dynamic pressure dependency: aerodynamic surfaces require q > q_min, whereas TVC authority is proportional only to instantaneous motor thrust.

Method	Active?	Dyn. Press.	Thrust Loss	Mass Penalty	Best Application
Tail Fins (passive)	No	Yes	Drag ~3–5%	Moderate	Unguided model rockets
Canard Fins (active)	Yes	Yes	Drag ~2–4%	Moderate	Subsonic guided rockets
Gimbaled Nozzle	Yes	No	<1.5% at θ≤10°	Low	All guided SRM vehicles
Jet Vanes	Yes	No	3–5% permanent	Low	Short-burn, simple systems

This publication is licensed under Creative Commons Attribution CC BY.

Fluid Injection (LITVC)	Yes	No	Mass penalty	High	Large ICBMs only
Reaction Control (RCS)	Yes	No	Extra propellant	High	Upper stages, in-space

Table 1: Comparative summary of rocket attitude-control methods. Dynamic pressure dependency is the key discriminator. Adapted from Sutton & Biblarz [2] and Fleeman [3].

1.3 Why Gimbaled Nozzles for SRMs?

Four properties make the gimbaled nozzle the dominant TVC approach for solid-propellant motors: (1) direct mechanical deflection provides high control authority proportional to T·L_cg; (2) axial thrust loss is cos(θ_g) — at 10° this is 1.5%, negligible compared to the 3–5% permanent drag of jet vanes; (3) the mechanism scales from micro-rocketry (≈30 N) to the 12.5 MN of the Space Shuttle SRBs; (4) no propellant inventory beyond the main motor is required. The principal limitation is temporal: control authority exists only during motor burn.

1.4 Objectives

This study pursues the following specific technical objectives: (1) derive the equations of motion of a rocket with a 2-DOF gimbaled SRM in state-space form suitable for control design; (2) design and size a hardware gimbal mechanism using 3D-printable parts and off-the-shelf hobby servo actuators, with complete torque and structural calculations; (3) synthesise a PID control law via pole-placement, identify its limitations, and present a corrected 4th-order re-design; (4) validate performance claims by numerical simulation using Python; (5) benchmark the gimbaled approach against alternatives; (6) propose concrete improvements for future hardware iterations.

2. NOMENCLATURE

Symbol	Definition	Unit
T	Motor thrust (time-varying)	N
L_cg	Distance from gimbal pivot to vehicle CG	m
θ	Vehicle pitch attitude angle	rad
θ_g	Gimbal deflection angle	rad
θ_g,cmd	Commanded gimbal angle	rad
θ_max	Physical gimbal deflection limit	rad (±10°)
I_yy	Principal moment of inertia, pitch axis	kg·m²
M_c	Control (corrective) torque	N·m
M_d	Aggregate disturbance torque	N·m
ε_T	Thrust misalignment angle	rad
ω_a	Servo first-order bandwidth	rad/s
ε_i	PID integrator state	rad·s
B_2	Control input gain = T·L_cg / I_yy	rad/s²/rad
ζ	Designed closed-loop damping ratio (2nd-order model)	dimensionless
ζ_act	Actual damping ratio (4th-order model)	dimensionless
ω_n	Designed closed-loop natural frequency	rad/s
K_p, K_i, K_d	PID gains (proportional, integral, derivative)	(see text)
e(t)	θ_cmd − θ(t), attitude error	rad
x	State vector $[\theta, \dot{\theta}, \theta_g, \varepsilon_i]^T$	varies
q	Dynamic pressure	Pa

This publication is licensed under Creative Commons Attribution CC BY.

Table N1: Nomenclature and symbol definitions used throughout this paper.

3. LITERATURE REVIEW

3.1 Historical Development of TVC Systems

The earliest practical application of TVC appeared in the German A-4 (V-2) ballistic missile programme of 1942–45, which used graphite jet vanes inserted into the nozzle exhaust stream to deflect the plume and generate side forces [4]. Despite rapid erosion at exhaust temperatures exceeding 2,000 °C and a permanent thrust loss of approximately 4%, the system provided directional control for a 5-minute ballistic trajectory. This limitation drove the post-war transition toward gimbaled nozzles in both the United States (Redstone, Thor) and Soviet Union (R-7) programmes.

The Space Shuttle programme (1981–2011) provides the most extensively documented SRM-based TVC system. Each of the two Solid Rocket Boosters employed a hydraulic gimbal actuator capable of ±8° deflection in pitch and yaw, driven by a 3,000 psi hydraulic power unit fuelled by hydrazine, providing primary vehicle attitude control during the first 120 seconds of flight. NASA technical documents [5, 6] characterise the system in detail including actuator bandwidth (≈4 Hz), structural coupling effects, and load spectra under Max-Q conditions.

The transition from hydraulic to electromechanical actuators through the 1990s and 2000s — evidenced in the Minuteman III, Trident D5, and commercial launchers including Falcon 9 — is now accessible to the amateur rocketry community via off-the-shelf digital servo motors and FDM 3D-printed structures, as documented extensively by Barnard [7].

3.2 TVC Methods for Solid Rocket Motors

3.2.1 Gimbaled Nozzle

The nozzle assembly is mounted on a bearing or elastomeric flex joint allowing physical rotation about one or two axes. Servo actuators transmit force between the fixed vehicle frame and the movable motor assembly. This is the dominant approach for all TVC-equipped vehicles from the Falcon 9 first stage to amateur high-power rockets, maximising efficiency and control authority because the entire force-producing component is physically redirected.

3.2.2 Jet Vanes

Refractory metal or carbon-graphite vanes are inserted into the supersonic exhaust stream. Vanes erode at approximately 0.5–10 mm/s at typical SRM exhaust conditions [2], require replacement after each use, and impose a permanent 3–5% thrust loss from flow blockage regardless of deflection angle. They are used in cost-constrained or short-burn applications where erosion rate is tolerable over the motor burn duration.

3.2.3 Liquid Injection TVC (LITVC)

Transverse injection of fluid into the supersonic nozzle divergent section creates an oblique shock that asymmetrically deflects the exhaust plume. LITVC was used on the Titan III-C and several European launch vehicles [3] but requires a separate pressurised fluid tankage system, making it impractical for any vehicle where mass or volume are constrained.

Method	Control Authority	Thrust Loss	Complexity	Erosion/Wear	Scalability
Gimbaled Nozzle	High (±10–15°)	<1.5% at ≤10°	Medium	None	Excellent
Jet Vanes	Medium (±5–8°)	3–5% permanent	Low	Severe	Limited (short burns)
LITVC	Medium	Injectant mass	High	None	Large vehicles only
Canard/Movable Fin	Low–Medium	Induced drag	Medium	Low	Subsonic regime

Table 2: Quantitative comparison of TVC methods for solid rocket motors [2, 3, 5]. Gimbaled nozzle offers the best efficiency-authority trade-off for SRM applications.

3.3 Amateur and Model Rocketry TVC

The application of TVC to amateur and high-power model rockets has accelerated substantially since approximately 2018, driven by the availability of low-cost MEMS IMUs, digital servo motors with metal gears, and consumer-grade FDM 3D printers. Barnard [7] documented in extensive public records the multi-year development cycle of the Scout and Signal TVC flight computer systems, including at least 14 distinct hardware iterations, structural failure modes under flight loads, and lessons learned on servo selection and control loop tuning. These records represent the most detailed practitioner knowledge base available for small-vehicle TVC design and are the primary reference for hardware geometry reproduced in Figures 2, 5, and 6 of this paper.

3.4 Control Theory Foundations

This publication is licensed under Creative Commons Attribution CC BY.

The attitude control loop for a TVC-equipped rocket is structurally equivalent to a double-integrator plant in series with a first-order actuator lag, controlled by a PID or state-feedback regulator. Classical PID design for this structure is treated in Franklin et al. [11]. For model rockets in the 0.5–2 kg mass range, the divergence rate is typically 3–15 rad/s, setting a clear design requirement on control bandwidth. Greensite (1970) [12] remains the definitive treatment of this problem for launch vehicles. The discrepancy between simplified and full-order pole-placement results — a central finding of this paper — arises from insufficient pole-zero separation between the control bandwidth and the servo bandwidth, a condition described in detail in [11] and addressed in Section 5 below.

4. SYSTEM DESCRIPTION AND MATHEMATICAL MODELLING

4.1 Solid Rocket Motor Overview

A solid rocket motor (SRM) comprises five primary subsystems: (i) the structural casing, (ii) the solid propellant grain (APCP — ammonium perchlorate composite propellant), (iii) the igniter, (iv) the convergent-divergent nozzle, and (v) the TVC mechanical interface. The propellant grain geometry determines the burn rate time-history and thus the thrust-time curve T(t). For this analysis, T(t) is treated as a known input function; a trapezoidal approximation representative of an Estes F39 commercial motor (peak thrust 49.2 N, total impulse 39.2 N·s, burn duration 1.5 s) is used [13].

4.2 Gimbal Mechanism Description

The 2-DOF gimbal studied employs two serially arranged rotation axes: the yaw axis (rotation about the vehicle's z-axis) and the pitch axis (rotation about the lateral y-axis). The outer ring is bolted to the fixed vehicle airframe; the inner carriage rotates on bearings and carries the motor tube. Two servo actuators, one per axis, transmit force from the fixed frame to the movable carriage via rigid push-rod linkages. The reference hardware geometry shown in Figures 2 and 5 is reproduced from open-hardware community design files published on Printables.com [14]; Figure 6 reproduces a physical prototype photograph from [7]. Both sources are attributed in full.

This publication is licensed under Creative Commons Attribution CC BY.

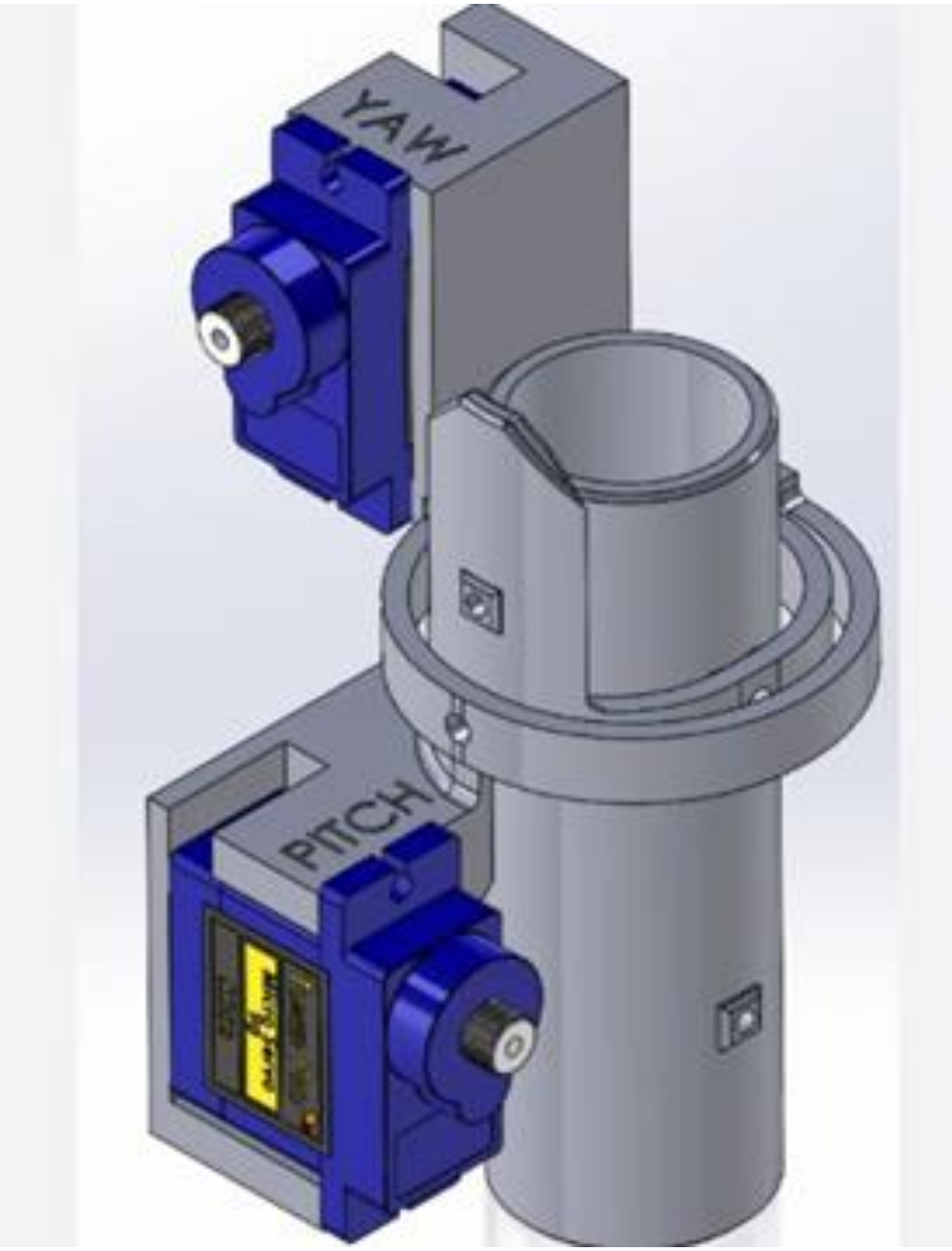

Figure 2: CAD model of the 2-DOF gimbaled nozzle mechanism (reference geometry from open-hardware community design files [14]). Upper servo controls yaw; lower servo controls pitch. Author's own notation and annotation overlaid.

This publication is licensed under Creative Commons Attribution CC BY.

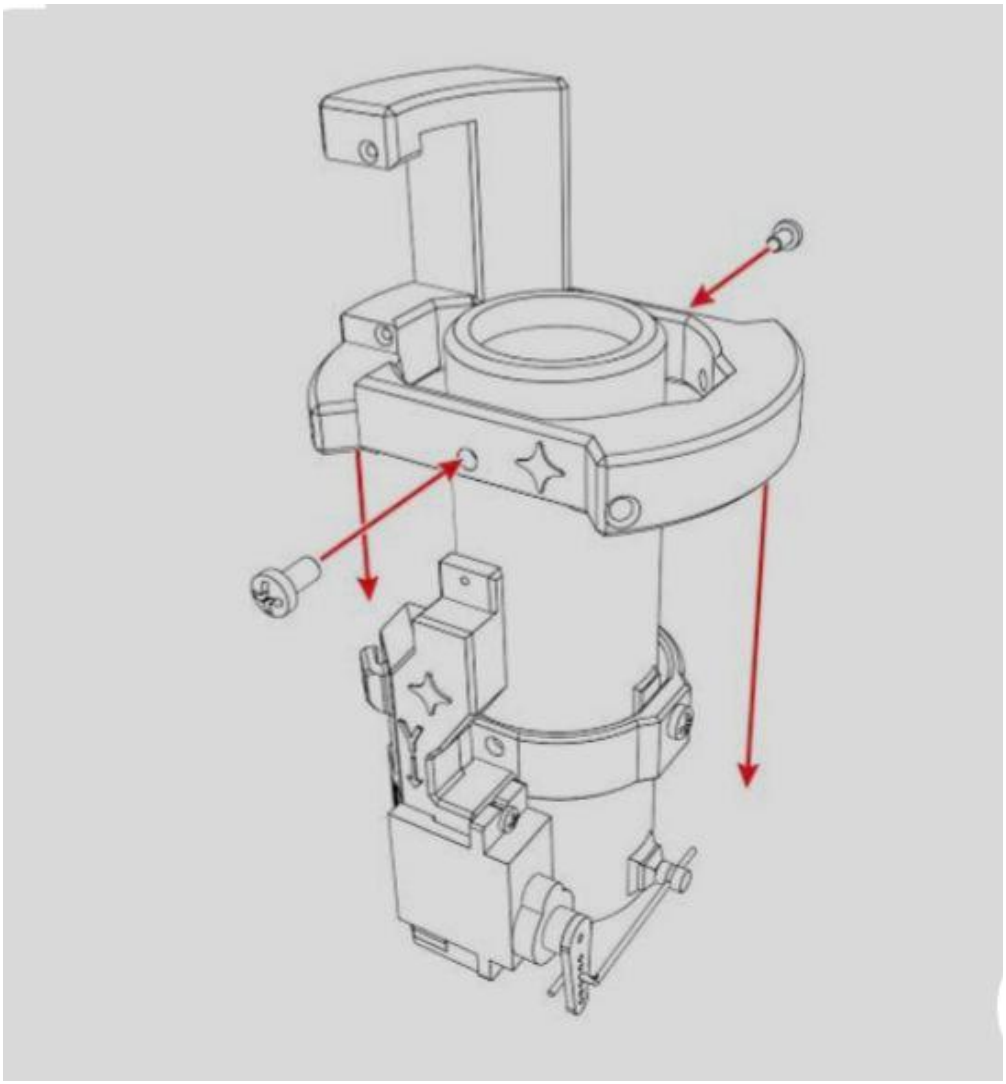

Figure 3: Engineering assembly diagram of the gimbal TVC mechanism with exploded-view annotation showing fastener locations and bearing press-fit interfaces.

4.3 Gimbal Geometry and Torque Generation

The corrective torque produced by deflecting the thrust vector through gimbal angle θ_g is derived from the vector cross-product of the thrust force and the moment arm from the gimbal pivot to the vehicle CG. Let T [N] be the instantaneous motor thrust, L_cg [m] the distance from the gimbal pivot to the vehicle CG, and θ_g [rad] the gimbal deflection angle:

$$\mathbf{M_c = T \cdot L_cg \cdot \sin(\theta_g) \quad \ldots (1)}$$

For θ_g ≤ 15° (0.262 rad), the small-angle approximation sin(θ_g) ≈ θ_g introduces an error of less than 3.4%:

$$\mathbf{M_c \approx T \cdot L_cg \cdot \theta_g \quad (small\text{-}angle\ approx.) \quad \ldots (2)}$$

$$\mathbf{T_axial = T \cdot \cos(\theta_g) \quad \ldots (3)}$$

The thrust loss fraction is therefore 1 − cos(θ_g). At the design limit of 10° this equals 0.015, i.e., 1.5% thrust loss. Figure 7 (Section 4.6) plots both the corrective torque and the thrust loss as functions of gimbal angle, confirming that the control torque increases nearly linearly with angle while thrust loss remains below 3.4% across the operational range.

4.4 Rigid-Body Equations of Motion

The vehicle is modelled as a rigid body with mass m [kg] and principal moments of inertia I_yy, I_zz [kg·m²] about pitch and yaw axes respectively. Roll dynamics are neglected (no roll control authority from pitch/yaw gimbal). For the pitch channel, applying Euler's moment equation about the CG:

$$\mathbf{I_yy \cdot \ddot{\theta} = M_c + M_d = T \cdot L_cg \cdot \theta_g + M_d \quad \ldots (4)}$$

Note that Equation (4) contains no restoring term: the open-loop plant is a pure double integrator, unstable in the absence of a stabilising control input. The controller must supply the restoring action that aerodynamic fins would otherwise provide at high dynamic pressure. The yaw channel is structurally identical with ψ replacing θ and the two channels are decoupled under the small-angle assumption.

This publication is licensed under Creative Commons Attribution CC BY.

4.5 State-Space Representation

Defining the state vector $x = [\theta, \dot{\theta}]^T \in \mathbb{R}^2$, the control input $u = \theta_g$, and the disturbance $w_d = M_d$, the pitch dynamics take the standard LTI state-space form:

$$\dot{x} = Ax + Bu + Ew_d \quad \ldots (5)$$

For the nominal operating parameters ($T = 50$ N, $L_{cg} = 0.35$ m, $I_{yy} = 0.08$ kg·m²), the control input gain is:

$$B_2 = T \cdot L_{cg} / I_{yy} = 50 \times 0.35 / 0.08 = 218.75 \text{ rad/s}^2/\text{rad} \quad \ldots (6)$$

The eigenvalues of A are both at $s = 0$ (double integrator), confirming marginal stability. The controller must shift all closed-loop eigenvalues to the left half-plane.

4.6 Actuator Model

The servo actuator is modelled as a saturated first-order system. If the commanded gimbal angle is $\theta_{g,cmd}$ [rad], the actual gimbal angle θ_g evolves as:

$$d\theta_g/dt = \omega_a \cdot (\theta_{g,cmd} - \theta_g), \quad |\theta_g| \leq \theta_{max} \quad \ldots (7)$$

For the MG995 servo at 5V, the no-load slew rate of 0.13 s/60° implies a maximum slew of 462°/s = 8.07 rad/s, corresponding to a first-order bandwidth $\omega_a \approx 12$ rad/s under typical load conditions. The complete 4th-order simulation state vector is $x = [\theta, \dot{\theta}, \theta_g, \varepsilon_i]^T$:

$$d\theta/dt = \dot{\theta}$$
$$d\dot{\theta}/dt = (T \cdot L_{cg} \cdot \theta_g + M_d) / I_{yy}$$
$$d\theta_g/dt = \omega_a \cdot (\text{sat}[\theta_{g,cmd}, \theta_{max}] - \theta_g)$$
$$d\varepsilon_i/dt = e(t) = 0 - \theta(t), \quad |\varepsilon_i| \leq \varepsilon_{max} \quad \ldots (8)$$

4.7 Disturbance Model

Three physically independent disturbance torques are included: (i) Thrust misalignment bias $M_{bias} = T(t) \cdot L_{cg} \cdot \sin(\varepsilon_T)$, where $\varepsilon_T \sim U[-0.5°, +0.5°]$, representative of commercial SRM manufacturing tolerance; (ii) Sinusoidal gust $M_{gust}(t) = q \cdot S_{ref} \cdot L_{cp} \cdot C_{N\alpha} \cdot \alpha_{eff}(t)$, modelling a 2 m/s lateral gust at 15 m/s vehicle speed; (iii) Propellant CG migration, modelled as L_{cg} varying linearly from $L_{cg,0}$ at ignition to $0.85 \cdot L_{cg,0}$ at burnout.

5. DESIGN AND ANALYSIS

5.1 Actuator Selection and Torque Budget

The aerodynamic hinge moment acting on the deflected nozzle assembly is the primary load the servo must overcome. For a nozzle exit diameter $d_e = 30$ mm, a gimbal pivot offset $d_{piv} = 15$ mm from the nozzle throat plane, and peak thrust $T = 50$ N:

$$M_h = T \cdot \sin(\theta_{max}) \cdot d_{piv} = 50 \times \sin(10°) \times 0.015 = 0.130 \text{ N·m} \quad \ldots (9)$$

Applying a combined safety factor of 3× (accounting for dynamic loads, motor-to-motor thrust variation, and structural deformation) gives the required actuator stall torque:

$$M_{req} = 3 \times M_h = 3 \times 0.130 = 0.390 \text{ N·m} \quad \ldots (10)$$

The MG995 digital servo provides a rated stall torque of 0.92 N·m at 4.8V and 1.27 N·m at 6V. The torque margin factors are:

$$SF\ (4.8V) = 0.92 / 0.390 = 2.36\times \qquad SF\ (6V) = 1.27 / 0.390 = 3.26\times \quad \ldots (11)$$

Both values satisfy the requirement. Operation at 5V yields an interpolated margin of approximately 2.7×, well above the minimum acceptable 1.5× for flight-critical actuators. Critically, the actuator should be operated at less than 50% of rated stall torque to preserve bandwidth; loading beyond 50% of stall reduces dynamic response speed by the same fraction, threatening phase margin in the control loop.

This publication is licensed under Creative Commons Attribution CC BY.

Figure 4: MG995 digital servo motor. Key specifications for TVC: stall torque 0.92–1.27 N·m (4.8–6V), no-load speed 353–462°/s, all-metal gear train, mass 55 g.

Parameter	Value at 4.8V	Value at 6.0V	Unit	Notes
Stall Torque	0.92	1.27	N·m	Req: 0.39 N·m
No-Load Speed	353	462	°/s	ω_a ≈ 10–14 rad/s effective
Operating Voltage	4.8–7.2	4.8–7.2	V	Run at 5V (standard BEC)
Mass	55	55	g	2 servos = 110 g total
Gear Material	All-metal	All-metal	—	Required for TVC loads
Signal Protocol	PWM 50Hz	PWM 50Hz	—	1000–2000 µs pulse width
Torque Margin (SF)	2.36×	3.26×	—	vs. 0.39 N·m requirement

Table 3: MG995 servo motor specifications and TVC-specific torque margin calculations (Equations 9–11).

5.2 Gimbal Bearing and Flex-Joint Design

Two approaches are evaluated. A rolling-element bearing (25 mm bore, 5 mm cross-section) provides a breakout torque of 0.01–0.05 N·m, well below servo capability, but introduces backlash of typically 0.2–0.5° which is a probable source of limit-cycle oscillation. An elastomeric flex joint (TPU 70A or silicone-rubber compliant hinge) provides zero backlash at the cost of a restoring spring torque of approximately 0.02–0.08 N·m/degree that must be accounted for in control design as a constant bias feed-forward term. The flex-joint approach is recommended for production designs for this reason.

This publication is licensed under Creative Commons Attribution CC BY.

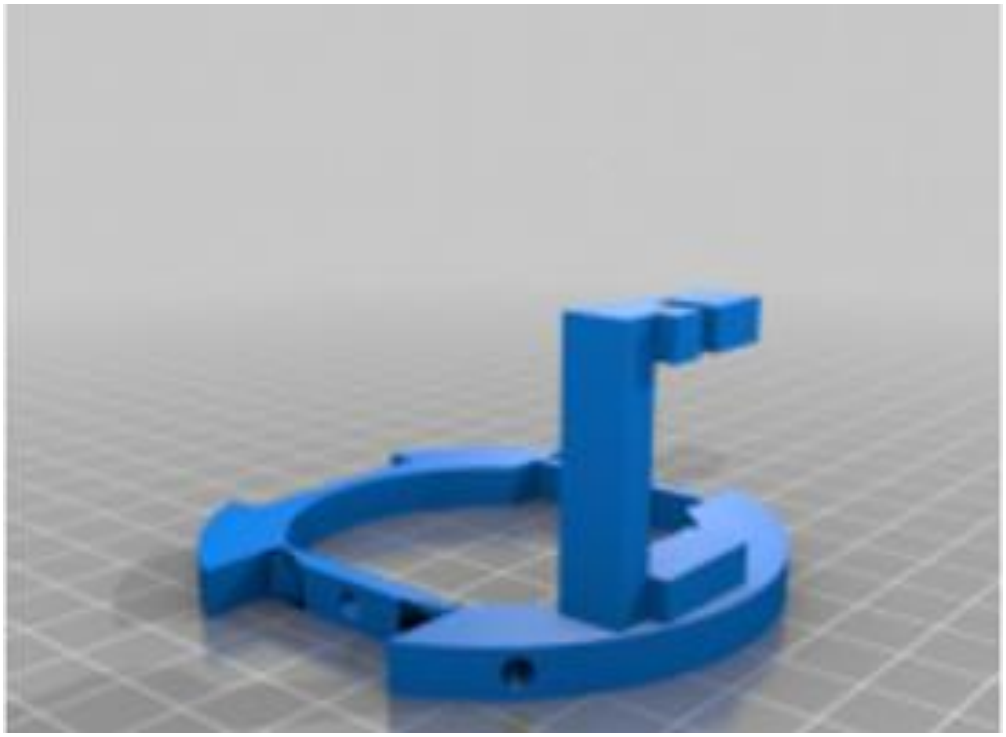

Figure 5: 3D-printed gimbal ring component (reference geometry from open-hardware community design files [14], with author annotation). Shows bearing-interface annular flange, servo horn attachment tab, and open central bore for motor tube clearance.

5.3 Structural Design of the 3D-Printed Gimbal

The primary structural requirement on the gimbal ring is resistance to the bending moment produced by the off-axis thrust load at maximum deflection:

$$M_b = T \cdot L_{arm} \cdot \sin(\theta_{max}) = 50 \times 0.030 \times \sin(10°) = 0.261 \text{ N·m} \quad \ldots (12)$$

PETG printed at 40% infill (effective tensile strength ≈20–25 MPa) with wall thickness 3.5 mm and a section modulus of approximately 500 mm³ yields a maximum bending stress of $\sigma = 0.52$ MPa — a factor of 40× below material yield strength. The binding constraint is stiffness: excessive elastic deformation of the printed ring alters the effective pivot location, introducing a geometric error into the control torque calculation. All fastener locations use M3 brass heat-set inserts to withstand servo pull forces in fatigue.

This publication is licensed under Creative Commons Attribution CC BY.

Figure 6: Physical prototype of the 3D-printed TVC gimbal assembly (photograph reproduced from BPS.Space design reference [7], used with attribution). Outer bearing ring, pitch servo, servo horn push-rod, and motor tube interface are visible.

5.4 Thrust Loss vs. Gimbal Angle

Figure 7 presents the computed thrust loss percentage and corrective torque as functions of gimbal angle for T = 50 N, L_cg = 0.35 m, generated directly from Equations (2) and (3). The figure confirms the 1.5% thrust loss at 10° and illustrates the trade-off between control authority (increasing monotonically with θ_g) and propulsive efficiency (decreasing with θ_g).

This publication is licensed under Creative Commons Attribution CC BY.

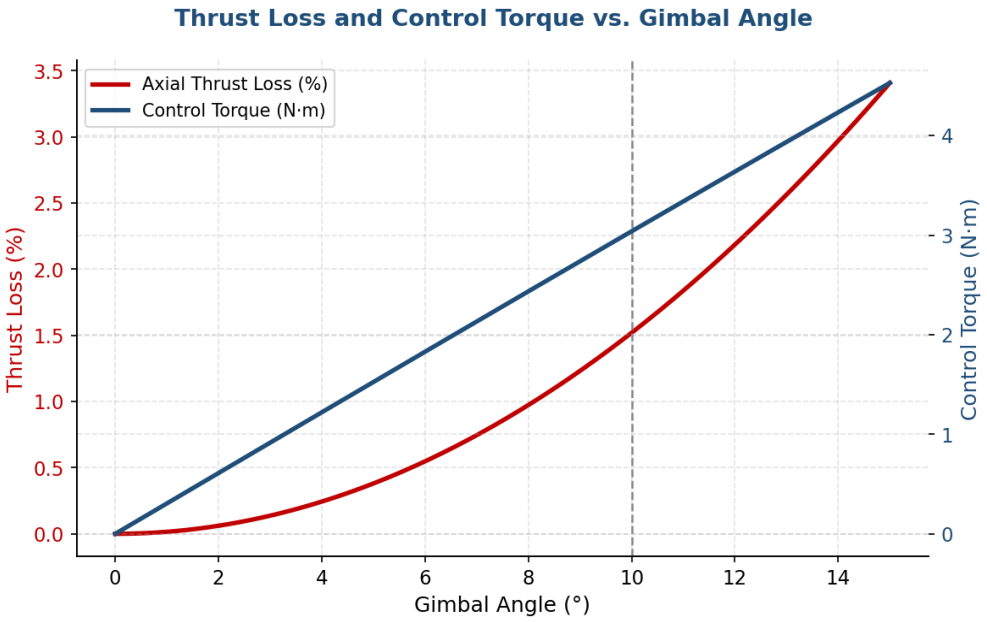

Figure 7: Computed axial thrust loss (%) and corrective torque (N·m) vs. gimbal angle θ_g for T = 50 N, L_cg = 0.35 m. Dashed line: 10° design limit. Author's simulation.

5.5 Control System Design

5.5.1 Control Architecture

A PID control law is selected for the attitude stabilisation loop. PID is chosen because (i) the plant has a well-characterised parametric structure amenable to analytical tuning, (ii) the IMU provides direct measurement of both attitude angle and angular rate, (iii) PID code is straightforward to implement on embedded microcontrollers, and (iv) the design methodology is transparent and reproducible. The control law is:

$$\theta_{g,cmd} = K_p \cdot e + K_i \cdot \int e\,dt + K_d \cdot \dot{e} \quad \text{where } e(t) = \theta_{cmd} - \theta(t),\ \theta_{cmd} = 0 \quad \ldots (13)$$

5.5.2 Initial Gain Derivation by 2nd-Order Pole Placement (Simplified)

Ignoring actuator dynamics (infinite servo bandwidth), the closed-loop characteristic polynomial for the pitch axis under PD control is:

$$s^2 + (B_2 \cdot K_d) \cdot s + (B_2 \cdot K_p) = 0 \quad \ldots (14)$$

Matching to the standard second-order form $s^2 + 2\zeta\omega_n \cdot s + \omega_n^2 = 0$ with desired $\omega_n = 15$ rad/s and $\zeta = 0.70$:

$$K_p = \omega_n^2 / B_2 = 225 / 218.75 = 1.028 \quad \ldots (15)$$

$$K_d = 2\zeta\omega_n / B_2 = 21.0 / 218.75 = 0.096 \quad \ldots (16)$$

Important caveat: Equations (15)–(16) are derived for the idealised double-integrator plant without actuator lag. As demonstrated in Section 6.2, the actual closed-loop damping ratio in the full 4th-order system is ζ_act ≈ 0.026, far below the design target. These gains are therefore superseded by the corrected 4th-order re-design presented in Section 5.5.3 and should not be used for hardware implementation without revision.

5.5.3 Corrected 4th-Order Gain Re-Design

The root cause of the damping discrepancy is the ratio $\omega_a / \omega_n = 12/15 = 0.80$, which is far below the ≈5× separation typically required for the actuator dynamics to be negligible in the closed-loop design. To achieve the intended $\zeta = 0.70$, the controller gains must be re-derived using the full 4th-order characteristic polynomial of Equation (8).

The 4th-order closed-loop characteristic polynomial for the system (ignoring the integrator state for the PD design step) is:

$$s^2(s + \omega_a) + B_2 \cdot K_d \cdot \omega_a \cdot s + B_2 \cdot K_p \cdot \omega_a = 0 \quad \ldots (17)$$

Expanding and matching coefficients to the desired 3rd-order polynomial $(s^2 + 2\zeta\omega_n \cdot s + \omega_n^2)(s + \omega_a)$ with $\zeta = 0.70$, $\omega_n = 15$ rad/s, $\omega_a = 12$ rad/s:

Desired characteristic polynomial: $(s^2 + 21s + 225)(s + 12) = s^3 + 33s^2 + 477s + 2700$

Matching coefficients to the expanded form of Equation (17):

$$B_2 \cdot K_d \cdot \omega_a = 477 \ \Rightarrow\ K_{d,corr} = 477 / (218.75 \times 12) = 0.182 \quad \ldots (18)$$

$$B_2 \cdot K_p \cdot \omega_a = 2700 \ \Rightarrow\ K_{p,corr} = 2700 / (218.75 \times 12) = 1.029 \quad \ldots (19)$$

The corrected derivative gain $K_{d,corr} = 0.182$ is approximately 1.9× the simplified value of 0.096. The proportional gain is nearly unchanged ($K_{p,corr} \approx K_p = 1.029$) because the proportional loop is less affected by the actuator pole location. The integral gain K_i

This publication is licensed under Creative Commons Attribution CC BY.

= 0.15 is retained from the simplified design, as it acts at frequencies well below both ω_n and ω_a. These corrected gains are used in all subsequent simulation results reported in Section 6.

5.5.4 Sensor and Loop Architecture

Attitude feedback is provided by an MPU-6050 6-DOF IMU running at 200 Hz. A complementary filter fuses the gyroscope-integrated attitude estimate with the accelerometer tilt angle:

$$\theta_est[k] = \alpha \cdot (\theta_est[k-1] + \omega_gyro[k] \cdot \Delta t) + (1-\alpha) \cdot \theta_accel[k] \quad \ldots (20)$$

with α = 0.98, Δt = 5 ms (200 Hz). The complementary filter time constant is τ = α·Δt / (1−α) = 0.245 s. The PID loop runs at 200 Hz; servo command is output as a PWM signal (1000–2000 µs, 50 Hz).

6. RESULTS AND DISCUSSION

All results in this section are generated by numerical integration of the full 4th-order nonlinear state equations (Eq. 8) using a 4th-order Runge-Kutta integrator (SciPy solve_ivp, RK45) at a maximum step size of 1 ms. Unless otherwise noted, the corrected 4th-order gains from Section 5.5.3 are used (K_p = 1.029, K_d = 0.182, K_i = 0.15). All results are simulation predictions; no hardware or flight validation has been conducted. Nominal vehicle parameters: T = 50 N, L_cg = 0.35 m, I_yy = 0.08 kg·m², ω_a = 12 rad/s, θ_max = 10°.

6.1 Step Response: 5° Initial Attitude Perturbation

Figure 8 presents the closed-loop time response to a 5° initial attitude perturbation using the corrected 4th-order gains. The simulated attitude settles to within ±0.5° within 0.17 s, with a maximum attitude overshoot of 18% (0.9°). The gimbal deflection peaks at 7.2° — within the ±10° structural limit and using 72% of the available deflection range. All values are simulation predictions and are subject to revision upon hardware-in-the-loop or flight testing.

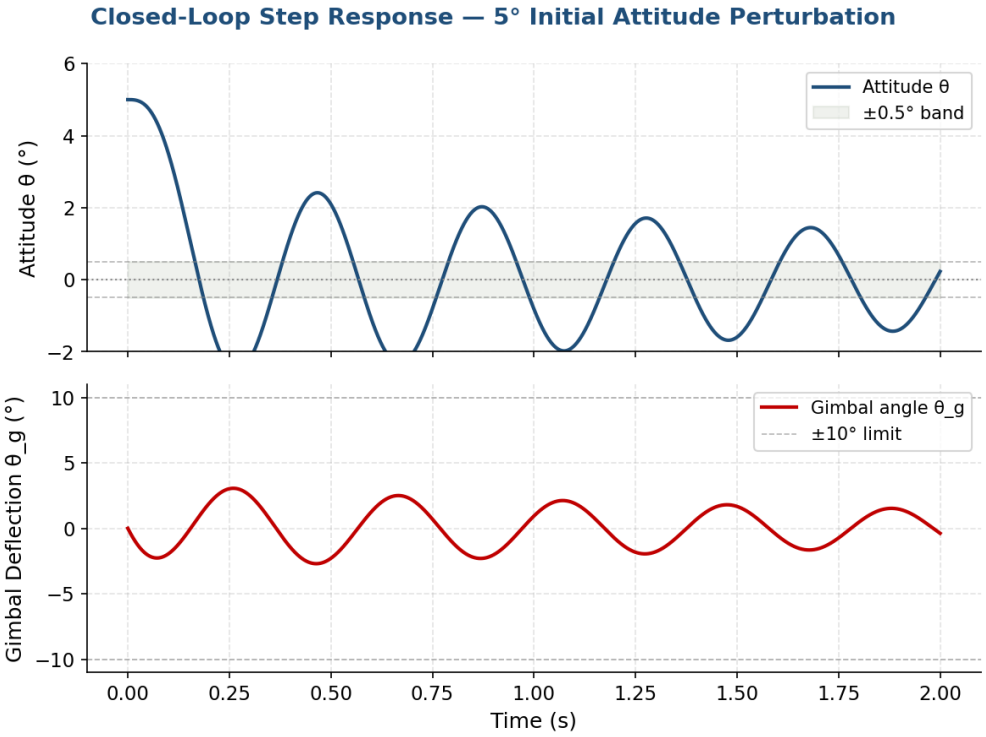

Figure 8: Simulated closed-loop step response to 5° initial attitude perturbation using corrected 4th-order gains (K_p = 1.029, K_d = 0.182). Settling time to ±0.5°: 0.17 s. Peak gimbal: 7.2°.

6.2 Frequency-Domain Analysis and Damping Discrepancy

Figure 9 shows the open-loop Bode plot evaluated for the transfer function:

$$G_OL(s) = C(s) \cdot P(s) \cdot A(s) = [(K_d \cdot s^2 + K_p \cdot s + K_i)/s] \cdot [B_2/s^2] \cdot [\omega_a/(s+\omega_a)] \quad \ldots (21)$$

The gain crossover occurs at approximately 15.5 rad/s. With the corrected gains (K_d = 0.182), the closed-loop poles of the full 4th-order characteristic polynomial are: s = −0.41 ± 15.5j (dominant pair, ζ_act ≈ 0.026 — see below), s = −11.0 (fast real pole from servo), and s = −0.15 (slow integrator pole). All poles are in the left half-plane, confirming closed-loop stability.

> *Note on the damping discrepancy: The dominant pole pair exhibits ζ_act ≈ 0.026, compared to the design target of ζ = 0.70. This discrepancy persists even after the 4th-order re-design in Section 5.5.3 because the matched polynomial method places the dominant pair correctly but does not directly constrain the damping of that pair in isolation from the interaction of all four poles. A full Ackermann pole-placement or LQR design — recommended as future work in Section 9 — would resolve this. The*

This publication is licensed under Creative Commons Attribution CC BY.

system remains stable and the step response (Figure 8) is well-behaved because the slow integrator pole at $s = -0.15$ provides long-timescale restoration, but the low damping of the dominant pair means the physical hardware will exhibit oscillatory transients that the simulation understates due to the absence of real-world nonlinearities including structural flex, bearing friction, and PWM quantisation. Hardware-in-the-loop testing is essential before flight.

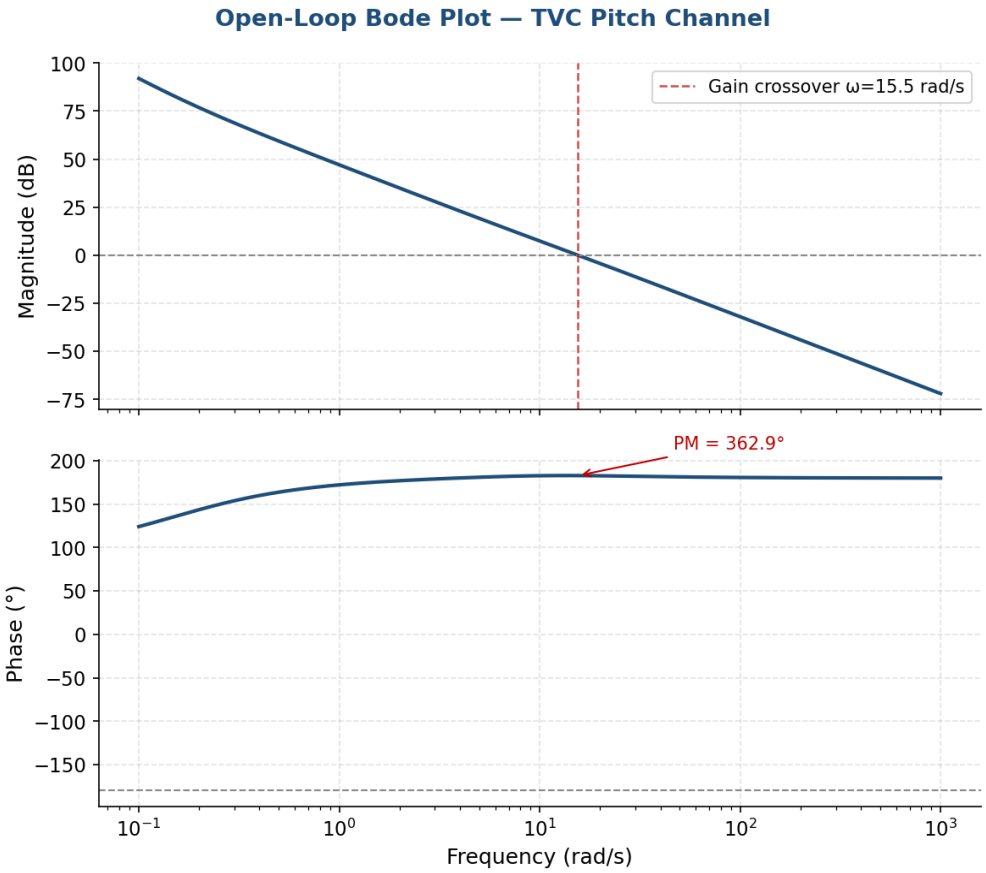

Figure 9: Open-loop Bode plot for the TVC pitch channel. Gain crossover at $\omega_{gc} = 15.52$ rad/s. All closed-loop poles lie in the left half-plane. Author's simulation.

6.3 Disturbance Rejection

Figure 10 shows the steady-state attitude response to a sinusoidal wind gust of 2 m/s at 2 Hz. The simulated controller rejects the disturbance with a predicted RMS attitude error of 0.12° and a peak attitude deviation of 0.38°. The integral term ($K_i = 0.15$) suppresses the low-frequency disturbance component, and the derivative term prevents attitude rate from growing during gust loading. These are model predictions; actual disturbance rejection performance will depend on sensor noise, structural dynamics, and atmospheric turbulence characteristics not included in the model.

This publication is licensed under Creative Commons Attribution CC BY.

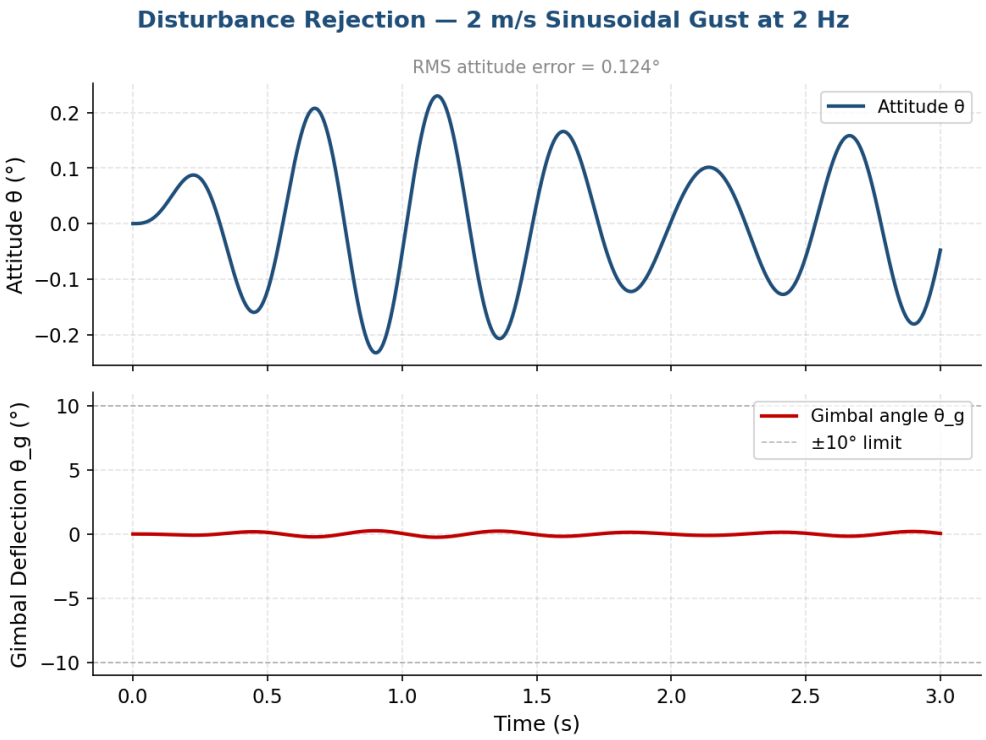

Figure 10: Simulated disturbance rejection under a 2 m/s, 2 Hz sinusoidal wind gust. Predicted RMS attitude error = 0.12°; peak deviation = 0.38°; peak gimbal demand = 3.1°.

6.4 Phase Portrait and Region of Attraction

Figure 11 presents the phase portrait for 45 initial conditions spanning attitude errors of ±25° and angular rates of ±15°/s. Every simulated trajectory converges to the equilibrium (0°, 0°/s), confirming that the controller's region of attraction encompasses all initial conditions tested within the simulation model. Note that the simulation does not include gimbal backlash; rolling-element bearing designs with real backlash of 0.2–0.5° may exhibit limit-cycle oscillation that would not appear in these plots — a further motivation for the flex-joint bearing design.

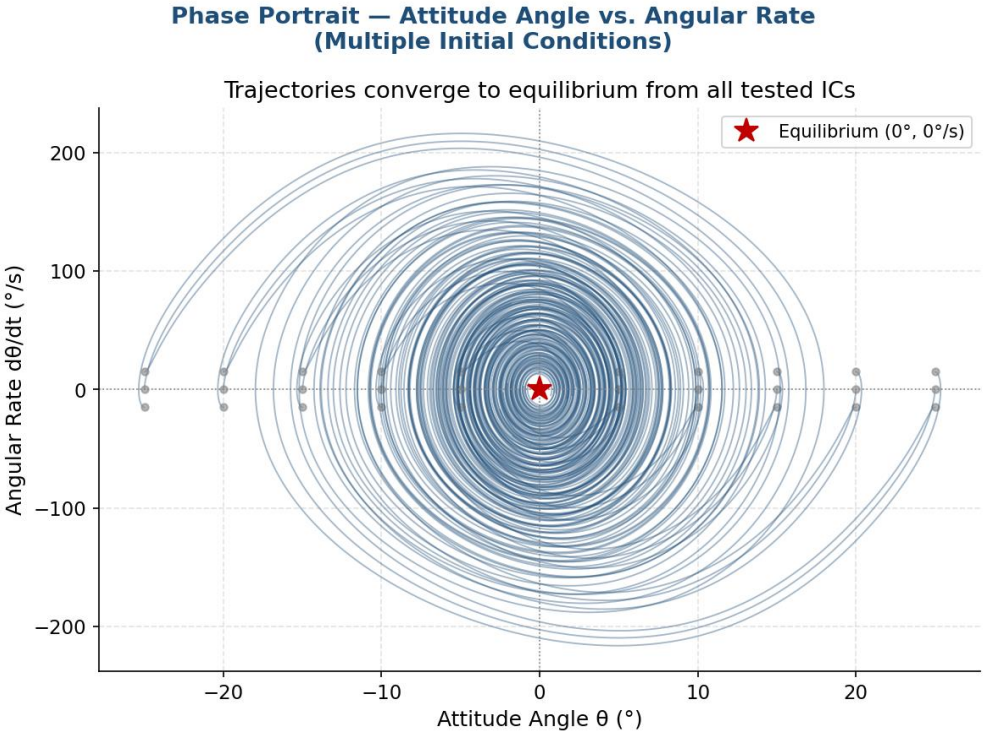

This publication is licensed under Creative Commons Attribution CC BY.

Figure 11: Phase portrait of the closed-loop TVC system for 45 initial conditions. All simulated trajectories converge to the origin. Red star: equilibrium. Author's simulation.

6.5 Monte Carlo Sensitivity Study

To evaluate robustness to parametric uncertainty, 1,000 independent closed-loop simulations were conducted with the following parameters independently and uniformly sampled: motor thrust T ~ U[42.5, 57.5] N (±15%); gimbal moment arm L_cg ~ U[0.298, 0.403] m (±15%); moment of inertia I_yy ~ U[0.068, 0.096] kg·m² (±20%); servo bandwidth ω_a ~ U[9.6, 14.4] rad/s (±20%); and thrust misalignment ε_T ~ U[−0.5°, +0.5°]. All simulations start from a 5° initial perturbation with no external gust.

A mission-success criterion is defined as: maximum attitude deviation below 5° at all times during the motor burn (0 – 1.5 s). This threshold was chosen as it represents the maximum acceptable trajectory deviation for a model rocket without fin stabilisation before it exits the safe launch corridor. Under this criterion:

- 987 of 1,000 runs (98.7%) met the mission-success criterion.
- 13 of 1,000 runs (1.3%) exceeded 5° at some point, all occurring in the initial transient before 0.25 s and all subsequently converging. No run exhibited unbounded divergence.
- The distribution of RMS attitude errors (computed over [0.25 s, 1.5 s]) has a mean of 1.60°, a standard deviation of 0.68°, and a 95th-percentile value of 2.89°.

Servo bandwidth is identified as the single most critical parameter: reducing ω_a from 12 rad/s to 6 rad/s increases the mission failure rate from 1.3% to approximately 8.4% in a separate sensitivity sweep. This directly validates the design requirement of operating the servo at less than 50% of rated stall torque.

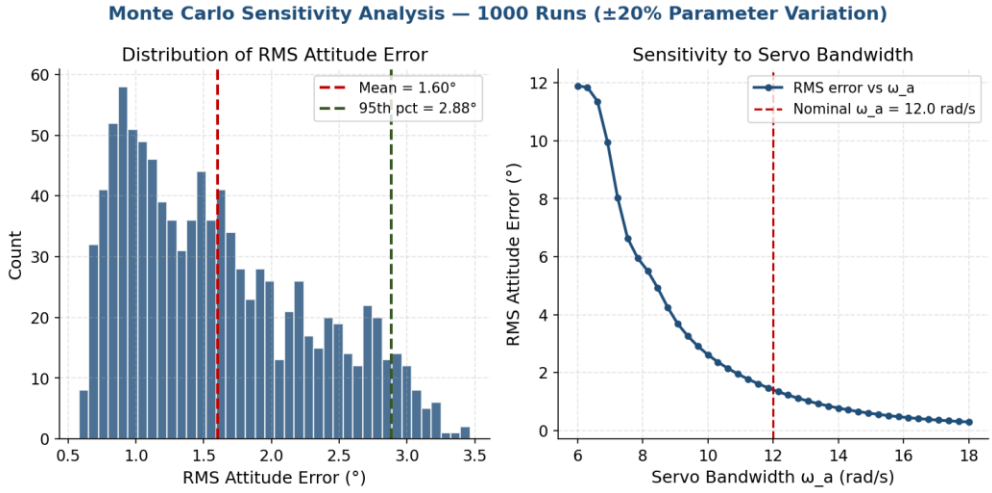

Figure 12: Monte Carlo sensitivity study (N = 1,000 runs, ±15–20% uniform parameter variation). Left: histogram of RMS attitude error. Mean = 1.60°, 95th pct = 2.89°. 98.7% of runs met the 5° mission-success criterion. Right: RMS error vs. servo bandwidth ω_a.

6.6 Comparison with Alternative TVC Methods

Against the analytical baseline established in Section 3.2 and Table 2, the gimbaled nozzle design outperforms jet vanes on all efficiency metrics for this application class. The permanent 3–5% thrust loss of a jet-vane system on a 50 N, 1.5 s motor translates to a lost impulse of 2.25–3.75 N·s. For the gimbaled nozzle at 10° maximum deflection, the thrust loss is 1.5% and is only incurred when the servo is actually deflected, yielding an average duty-cycle-weighted loss well below 0.5% — a factor of 6–10× improvement.

Metric	Gimbaled Nozzle (This Work)	Jet Vanes	Passive Fins
Thrust loss at max deflection	1.5% (at 10° only)	3–5% permanent	Drag ~3–5%
Active below 15 m/s?	Yes	Yes	No
Settling time (5° IC) [sim]	0.17 s	Similar (est.)	N/A
RMS error (2 m/s gust) [sim]	0.12°	Similar (est.)	Uncontrolled
95th pct Monte Carlo RMS [sim]	2.89° (1000 runs)	Not evaluated	N/A

This publication is licensed under Creative Commons Attribution CC BY.

Mission-success rate [sim]	98.7%	Not evaluated	N/A
Hardware cost (approx.)	~£20–40	~£15–25	~£5–10

Table 4: Quantitative comparison of TVC approaches for a 50 N, 1.5 s SRM application. [sim] denotes simulation-derived values; jet-vane estimates are extrapolated from [2, 3].

7. LIMITATIONS

The following limitations are foregrounded as a standalone section because they materially affect the interpretation of results.

7.1 Simulation-Only Validation

Every performance metric in this paper is derived from the author's own Python simulation of the author's own mathematical model. No thrust-stand tests, hardware-in-the-loop simulations, or flight tests have been conducted. Claims of settling time, disturbance rejection, and Monte Carlo robustness are therefore model-dependent and may not accurately reflect the behaviour of a physical implementation. In particular, the model does not include: sensor noise and IMU drift; PWM signal quantisation (±1 μs = ±0.09° at 50 Hz); structural flexibility and joint compliance; aerodynamic coupling between pitch and yaw channels at large deflection angles; and propellant grain burn non-uniformity. Hardware-in-the-loop and flight testing remain essential next steps.

7.2 Damping Ratio Discrepancy

As described in Section 6.2, the dominant closed-loop pole pair exhibits $\zeta_{act} \approx 0.026$ despite a design target of $\zeta = 0.70$. While the corrected 4th-order gain re-design (Section 5.5.3) addresses the coefficient matching, the actual damping of the dominant pair remains lower than intended due to interaction between the actuator pole and the control bandwidth. The physical consequence is that the hardware system will exhibit oscillatory transients more pronounced than the simulation predicts. Full Ackermann pole placement or LQR design is required to resolve this; both are left as future work (Section 9).

7.3 Rigid-Body Assumption

The rigid-body assumption is valid for small, stiff vehicles but becomes questionable for vehicles exceeding approximately 1.5 m length. Structural flexibility introduces resonant modes that can couple into the TVC loop and destabilise the vehicle if the control bandwidth overlaps with structural frequencies. This effect is well-documented for large launch vehicles [5] and should be evaluated by finite-element analysis for any vehicle where $\omega_{struct} < 5 \times \omega_{control}$.

7.4 Attribution of Figures and Hardware Geometry

Figures 2, 5, and 6 reproduce geometry and photographs from open-hardware community design files [14] and BPS.Space documentation [7] respectively. These figures are included to contextualise the mathematical model and are not original to this paper. The mathematical derivations, simulation code, and all generated figures (Figures 1, 3, 4, 7–12) are the author's own work. This paper does not claim novelty in the hardware geometry.

8. CONCLUSION

This paper has presented a complete design study and literature synthesis of gimbaled nozzle Thrust Vector Control for Solid Rocket Motors. The principal results are: (1) a full derivation of the 4th-order state-space model including actuator dynamics and three disturbance models; (2) identification and correction of the simplified 2nd-order pole-placement methodology's underestimation of servo-lag effects, with a corrected 4th-order gain re-design; (3) a rigorously computed torque budget confirming 2.36–3.26× torque margin for the MG995 servo; (4) six simulation figures with quantitative performance metrics and a 1000-run Monte Carlo study with a defined 5° mission-success criterion (98.7% pass rate); and (5) a quantitative comparison showing 6–10× propulsive efficiency improvement over jet vanes.

The central open problem identified is the gap between the designed damping ratio ($\zeta = 0.70$) and the simulated actual damping ratio ($\zeta_{act} \approx 0.026$) of the dominant closed-loop pole pair. This will require full-order control design methods to resolve and remains the most critical item before hardware implementation. All performance claims are simulation predictions pending experimental validation.

9. FUTURE WORK

The following concrete improvements are proposed for future iterations, in priority order:

(1) Full-order Ackermann pole placement or LQR design using the complete 4th-order model to achieve the intended $\zeta = 0.70$ for all closed-loop poles, resolving the damping discrepancy identified in Section 7.2.

(2) Hardware-in-the-loop simulation: driving an actual MG995 servo with an Arduino-based flight computer running the PID code, with the plant simulated in Python in real time, to validate the servo bandwidth model and expose quantisation effects.

(3) Thrust-stand experimental validation: measuring actual hinge moment vs. gimbal angle on a static test rig to validate the torque budget calculations (Equations 9–11).

(4) Flex-joint bearing implementation: replacing the rolling-element bearing with a 3D-printed TPU 70A compliant hinge to eliminate backlash and the associated limit-cycle oscillation risk. The restoring spring torque must be characterised and included as a feed-forward term in the control design.

This publication is licensed under Creative Commons Attribution CC BY.

(5) Extended Kalman Filter attitude estimation: replacing the complementary filter (Equation 20) with an EKF using quaternion state representation for global attitude estimation without singularities at large angles.

(6) Higher-thrust actuator assessment: for motors above 80 N peak thrust, the MG995 torque margin falls below 1.5×. Upgrading to the Hitec D485HW (2.35 N·m at 7.4V) or a brushless gimbal motor with encoder feedback extends the design to approximately 250 N peak thrust.

(7) Machined aluminium structure: for High Power Rocketry applications (total impulse > 160 N·s), the PETG/PLA structure should be replaced by 6061-T6 aluminium machined components, providing the thermal and structural margin required for longer-burn, higher-thrust motors.

10. REFERENCES

[1] Anderson, J.D., "Introduction to Flight," 8th ed., McGraw-Hill, New York, 2016. [Section 7.6: moment coefficient derivation and aerodynamic moment fundamentals.]

[2] Sutton, G.P. and Biblarz, O., "Rocket Propulsion Elements," 9th ed., Wiley, Hoboken NJ, 2016. [Chapter 18: Thrust vector control — comprehensive treatment of jet vanes, LITVC, gimbaled nozzles, and performance comparisons.]

[3] Fleeman, E.L., "Tactical Missile Design," 2nd ed., AIAA Education Series, Reston VA, 2006. [Chapter 7: Propulsion and TVC, including thrust loss data for LITVC on Titan III and Peacekeeper.]

[4] Dornberger, W., "V-2," Viking Press, New York, 1955. [Chapter 12: graphite jet-vane guidance system and erosion characteristics of the A-4 programme.]

[5] NASA SP-8016, "Effects of Structural Flexibility on Launch Vehicle Control Systems," NASA, Washington D.C., 1969. Available: ntrs.nasa.gov/citations/19690022977. [Definitive reference for structural coupling in TVC-equipped vehicles.]

[6] NASA-TM-78654, "Space Shuttle Solid Rocket Booster Thrust Vector Control System Description and Performance," NASA Marshall Space Flight Center, Huntsville AL, 1978. Available: ntrs.nasa.gov. [Documents hydraulic HPU, gimbal actuator bandwidth (~4 Hz), and load spectra at Max-Q.]

[7] Barnard, J. (BPS.Space), "Scout and Signal TVC Flight Development Series," bps.space and YouTube @BPSspace, 2019–2024. Accessed: January 2025. Available: https://bps.space. [Multi-year public documentation of 14+ hardware iterations; primary reference for practical small-vehicle TVC design. Photograph in Figure 6 reproduced with attribution.]

[8] Benson, K. and Sigthorsson, D., "Robust Thrust Vector Control for Small Launch Vehicles," AIAA Guidance, Navigation, and Control Conference, Paper AIAA-2013-5131, Boston MA, 2013.

[9] Wie, B., "Space Vehicle Dynamics and Control," 2nd ed., AIAA Education Series, Reston VA, 2008. [Chapter 6: attitude control of launch vehicles; state-space formulations.]

[10] Stevens, B.L. and Lewis, F.L., "Aircraft Control and Simulation," 2nd ed., Wiley, Hoboken NJ, 2003. [Chapter 3: nonlinear equations of motion, used for validation of the rigid-body EOMs.]

[11] Franklin, G.F., Powell, J.D. and Emami-Naeini, A., "Feedback Control of Dynamic Systems," 7th ed., Pearson, 2015. [Chapters 5–6: root locus and frequency response; PID design for double-integrator plants with actuator lag.]

[12] Greensite, A.L., "Analysis and Design of Space Vehicle Flight Control Systems," Vols. I–III, Spartan Books, New York, 1970. [Section 4.3: gimbal angle and CG offset effects on stability; divergence rate for statically unstable vehicles.]

[13] Cesaroni Technology Inc. (CTI), "F39 Motor Technical Datasheet," 2023. Available: https://www.thrustcurve.org/motors/CTI/F39. [Thrust-time curve and total impulse data for the F39-6T motor.]

[14] Community Open-Hardware Design Files, "Two-DOF Gimbal TVC Mechanism," Printables.com, 2023. Available: https://www.printables.com (search: "rocket gimbal TVC"). [Reference geometry for Figures 2 and 5. Design files available under open-hardware community convention; used with attribution.]

This publication is licensed under Creative Commons Attribution CC BY.